Physics in Medicine & Biology

PAPER

SiPM signal readout for inter-crystal scatter event identification in PET detectors

To cite this article: Haewook Park and Jae Sung Lee 2020 *Phys. Med. Biol.* **65** 205010

IOP Publishing Phys. Med. Biol. **65** (2020) 205010 https://doi.org/10.1088/1361-6560/aba8b4

Physics in Medicine & Biology

IPEM Institute of Physics and Engineering in Medicine

CrossMark

RECEIVED
12 May 2020

REVISED
20 July 2020

ACCEPTED FOR PUBLICATION
23 July 2020

PUBLISHED
15 October 2020

PAPER

SiPM signal readout for inter-crystal scatter event identification in PET detectors

Haewook Park[1,2] **and Jae Sung Lee**[2,3,4]

[1] Department of Biomedical Sciences, Seoul National University College of Medicine, Seoul 03080, Republic of Korea
[2] Department of Nuclear Medicine, Seoul National University College of Medicine, Seoul 03080, Republic of Korea
[3] Institute of Radiation Medicine, Medical Research Center, Seoul National University College of Medicine, Seoul 03080, Republic of Korea
[4] Brightonix Imaging Inc., Seoul 04782, Republic of Korea

E-mail: jaes@snu.ac.kr

Keywords: inter-crystal scatter (ICS), silicon photomultiplier (SiPM), positron emission tomography (PET), time-over-threshold (TOT)

Abstract

In positron emission tomography (PET) with pixelated detectors, a significant number of annihilation photons interact with scintillation crystals through single or multiple Compton scattering events. When these partial energy depositions occur across multiple crystal elements, we call them inter-crystal scatter (ICS) events. ICS events lead to incorrect localization of the annihilation photons, thereby degrading the PET image contrast, spatial resolution, and lesion detectability. The accurate identification of ICS events is the first essential step to improve the quality of PET images by rejecting ICS events or recovering ICS events without losing PET sensitivity. In this study, we propose a novel silicon photomultiplier (SiPM) readout method to identify ICS events in one-to-one coupled PET detectors with a reduced number of data acquisition channels. For concept verification, we assembled a PET detector that consists of a 16-channel SiPM array and 4×4 lutetium oxyorthosilicate (LSO) array with a 3.2 mm crystal pitch. The proposed SiPM readout scheme serializes the 16 SiPM anode signals into four pulse train outputs encoded with four increasing time-delays in steps of 250 ns intervals. A *Sum* signal of the 16 SiPM anodes provides the timing information for time-of-flight measurement and a trigger signal for coincidence detection. A time-over-threshold (TOT) method was applied for obtaining the energy information followed by a subsequent TOT-to-energy calibration. We successfully identified the ICS events and determined their interacted positions and deposited energies by analyzing the digital pulses from the four pulse train output channels. The occurrence rate of ICS events was 10.85% for the 4×4 PET detector module with 3.2 mm-pitch LSO crystals. The PET detector yielded an energy resolution of $10.9 \pm 0.6\%$ and coincidence timing resolution of 285 ± 12 ps FWHM. We expect that the proposed method can be a useful solution for alleviating the readout burden of SiPM-based PET scanners with ICS event identification capability.

1. Introduction

Positron emission tomography (PET) is a medical imaging device that visualizes the radiotracer distribution in a living body by superimposing the lines-of-responses (LORs) detected from 511 keV annihilation photon pairs (Phelps 2000, Lee 2012). A basic element of modern PET scanners is a detector module in which a monolithic crystal or pixelated crystal arrays are coupled with photosensor arrays, such as multichannel photomultiplier tubes (PMTs) or silicon photomultipliers (SiPMs) (Cherry and Dahlbom 2004, Lee 2012). In the PET system with pixelated detectors, a true LOR is recorded when the two 511 keV photons originated from a single annihilation event deposit their energies through a single crystal element in each PET detector module placed on the opposite sides. However, a significant number of the annihilation photons undergo single or multiple Compton scattering events within pixelated crystal arrays before the final photon interaction occurs, and we call them inter-crystal scatter (ICS) events (Rafecas *et al* 2003, Yamaya *et al* 2011, Abbaszadeh *et al* 2018, Lee *et al* 2020). ICS events lead to the misalignment of true LORs owing to incorrect localization of the annihilation photons, thereby degrading the PET image contrast, spatial resolution, and lesion detectability (Miyaoka and Lewellen 2000, Teimoorisichani and Goertzen 2019, Zhang *et al* 2019, Lee *et al* 2020).

In PET detectors, multiplexing readout schemes that utilize a charge division circuit are widely used. The multiplexing readout scheme allows for collecting scintillation photons over photosensor arrays using a smaller number of data acquisition (DAQ) channels than the photosensors and crystal elements (Siegel *et al* 1996, Hong *et al* 2008, Yamamoto *et al* 2013, Kwon and Lee 2014, Ko *et al* 2016, Pizzichemi *et al* 2016, Park *et al* 2017, Kuang *et al* 2018). The accurate positioning of ICS events using the multiplexing readout remains challenging as the event positioning is based on a energy-weighted mean of individual photon interactions within the pixelated detectors. Several event positioning algorithms, such as Bayesian estimation (Pratx and Levin 2009), maximum likelihood estimation (Shinohara *et al* 2014), or convex optimization (Lee *et al* 2018a), have been investigated to improve the accuracy of ICS event identification incorporated with multiplexing readout schemes; however, the performances are not sufficient to improve the PET image quality (Lee *et al* 2018a). Likewise, in monolithic PET detectors, several three-dimensional (3D) positioning algorithms combined with depth-of-interaction estimation (Bruyndonckx *et al* 2006, Müller *et al* 2019) have been investigated to improve the positioning accuracy, but their performances are also limited by ICS events (Maas *et al* 2009).

Therefore, an individual readout scheme is more commonly used to achieve better ICS event identification performance in pixelated PET detectors (Comanor *et al* 1996, Rafecas *et al* 2003, Ota *et al* 2017, Surti and Karp 2018). The individual readout of photosensors in combination with one-to-one coupled scintillation crystals allows us to record the deposited energy and its interacted position on an event-by-event basis with the best count-rate performance and minimal dead-time effects. Consequently, more accurate discrimination of ICS events from photoelectric (PE) absorption or scatter/escape (i.e. Compton scattering with a subsequent escape) events is possible based on the individual readout. However, the main challenge of the individual readout scheme is a development cost and complexity in DAQ electronics because it should handle several thousands of readout channels at a full-ring PET system.

The aim of this study is to develop a SiPM readout scheme that allows for identifying ICS events in one-to-one coupled PET detectors with a smaller number of DAQ channels than the individual readout method. In this manuscript, we have introduced the proposed SiPM readout method and demonstrated its feasibility by using a PET detector module that consists of a 4×4 SiPM array one-to-one coupled with 16 scintillation crystals. In addition, we have presented the results of ICS event identification capability and PET detector performances in terms of energy resolution and coincidence resolving time (CRT).

2. Materials and methods

2.1. PET detector

The PET detector investigated in this study consists of a 4×4 SiPM array that features a 3.2 mm sensor pitch (S14161-3050HS-04; Hamamatsu Photonics K.K., Japan). The SiPM array was one-to-one coupled to a 4×4 array of lutetium oxyorthosilicate (LSO) crystals (EPIC Crystal, China) with a single crystal dimension of $3.12 \times 3.12 \times 15$ mm^3. The pitch between the crystal elements was 3.2 mm that matches the dimension of the sensor pitch of SiPM array. We optically isolated all the 16 LSO crystals by wrapping them with a 65 μm-thick enhanced spectral reflector film (ESR; 3M, US) that allows for scintillation photons to be collected by each of the corresponding SiPM channels. The SiPM and LSO arrays were tightly coupled with each other using an optical grease with a refractive index of 1.465 (BC-630; Saint-Gobain, France) and acrylonitrile butadiene styrene frame constructed with a 3D printer (Mojo; Stratasys, US).

2.2. SiPM readout scheme for ICS event identification

The proposed SiPM readout scheme for ICS event identification is illustrated in figure 1. All 16 cathodes of the SiPM array were bound to the common power line with a ferrite bead and bypass capacitor. The bias voltage supplied to the SiPM array was 42.0 V which corresponds to an over voltage of approximately 4 V. The signals from 16 SiPM anodes were individually amplified via a high-speed current feedback amplifier (AD8000; Analog Devices, US) and fed into a fast comparator (ADCMP601; Analog Devices, US) to generate a digital pulse with an internal hysteresis of 2 mV. Each of the 16 digital pulses was then serialized into four pulse train outputs (i.e. *G1*, *G2*, *G3*, and *G4*) using a quadruple two-input OR logic gate (SN74F32; Texas Instruments, US) after introducing different time-delays that increased with a 250 ns interval (i.e. 0, 250, 500, and 750 ns). Active delay-line chips (DS1100-250+; Maxim Integrated, US) were used to introduce the time-delays. A *Sum* signal that combines all the 16 SiPM anodes (i.e. 16:1 multiplexing ratio) was generated

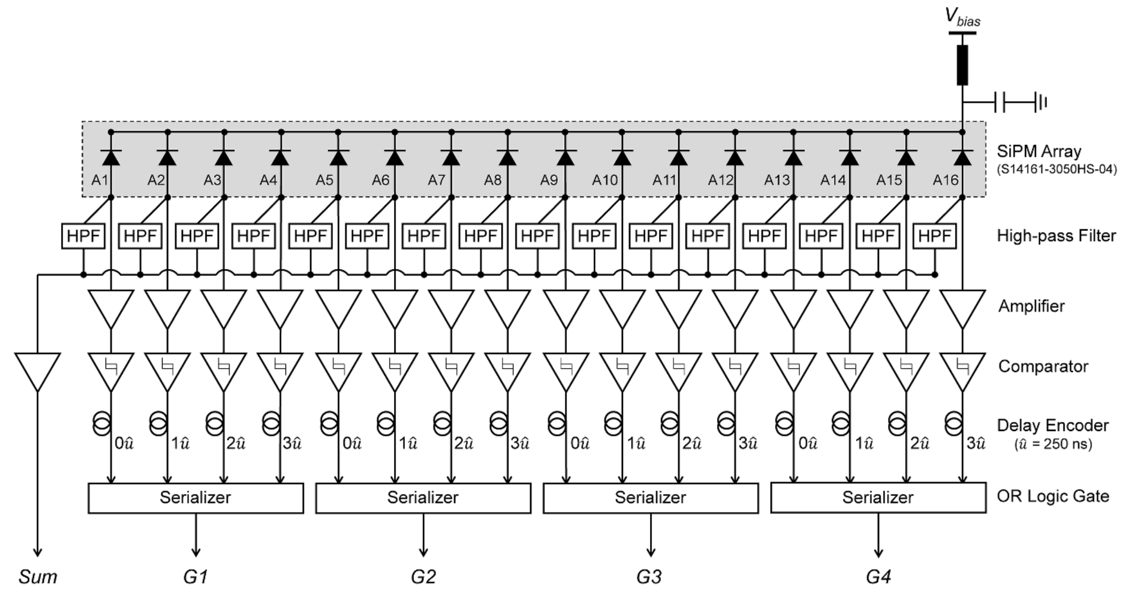

Figure 1. Schematic of the proposed SiPM readout for ICS event identification. The bias voltage was supplied to 16 SiPM channels via a common-cathode terminal. One branch of SiPM anodes was digitalized using a voltage comparator followed by a signal amplification stage and subsequently serialized into four pulse train outputs (i.e. *G1*, *G2*, *G3*, and *G4*) using an OR logic gate after introducing the different time-delays with a 250 ns increment. The other branch of SiPM anodes was used to generate a *Sum* signal after passing through a first-order HPF.

using an inverting summing amplifier (AD8000; Analog Devices, US). A first-order high-pass filter (HPF) was applied to each SiPM anode to enhance the CRT of the PET detector that requires time-of-flight (TOF) measurement capability.

2.3. Experimental setup and DAQ

Figure 2 shows the experimental setup used in this study. All the measurements were performed inside a thermostatic chamber at a fixed temperature of 20 °C. The four pulse train outputs outputs (i.e. *G1*, *G2*, *G3*, and *G4*) were fed into a domino-ring-sampler 4 (DRS4)-based digitizer (DT5742B; CAEN, Italy) that allows for the recording of 1024 waveform samples with a variable sampling rate of 0.75, 1, 2.5, and 5 GSPS. The pulse train outputs were sampled with a 1-GSPS sampling rate to ensure that the longest delayed events can be fully recorded. The *Sum* signal was branched into two routes using a custom-made fan-in/fan-out module that features an 8-fold signal amplification stage. One of the branched *Sum* signals was sampled with a 5-GSPS sampling rate for an off-line data analysis and the other branch was used for generating a coincidence trigger as an input for the DRS4 digitizer. The coincidence measurement was performed using a reference detector based on a Hamamatsu R9800 PMT coupled to a lutetium yttrium oxyorthosilicate crystal with a dimension of $4 \times 4 \times 10$ mm^3 (Lee *et al* 2011, Ito *et al* 2013). A single timing resolution (STR) of the reference detector was 220 ps FWHM. The detailed procedure of CRT measurement based on the reference detector and a series of nuclear instrumentation modules is described in Park and Lee (Park and Lee 2019). To avoid CRT measurement error due to the high-frequency signal crosstalk among the input channels of DRS4 chips, we conducted an inter-chip CRT measurement (Park *et al* 2018a). For energy and CRT measurements, we attached a ^{22}Na point source (MMS06-022; Eckert & Ziegler, Germany) with an activity of 3 μCi to the entrance window of reference detector and placed 10 cm away from the 4×4 PET detector module. A total 200 000 coincidence events were recorded for data analysis. A relatively long interval of the pulse train outputs would be a potential limitation of the proposed method; and therefore, we performed an initial high count-rate measurement by using multiple ^{22}Na point sources ($\sim$40 μCi) and placing them at a 1 cm distance (i.e. 10-fold close distance) from the 4×4 PET detector module. Here, we used the same experimental setup as illustrated in figure 2.

2.4. Data analysis

A discharged SiPM channel was identified based on the pre-defined time-delays (i.e. 0, 250, 500, and 750 ns) and pulse train output channels (i.e. *G1*, *G2*, *G3*, and *G4*) as summarized in table 1. A two dimensional (2D) flood map was generated based on a center-of-gravity algorithm, as described in equations (1) and (2), to verify the type of photon interactions. In those equations, $\hat{x}$ and $\hat{y}$ correspond to the estimated positions in

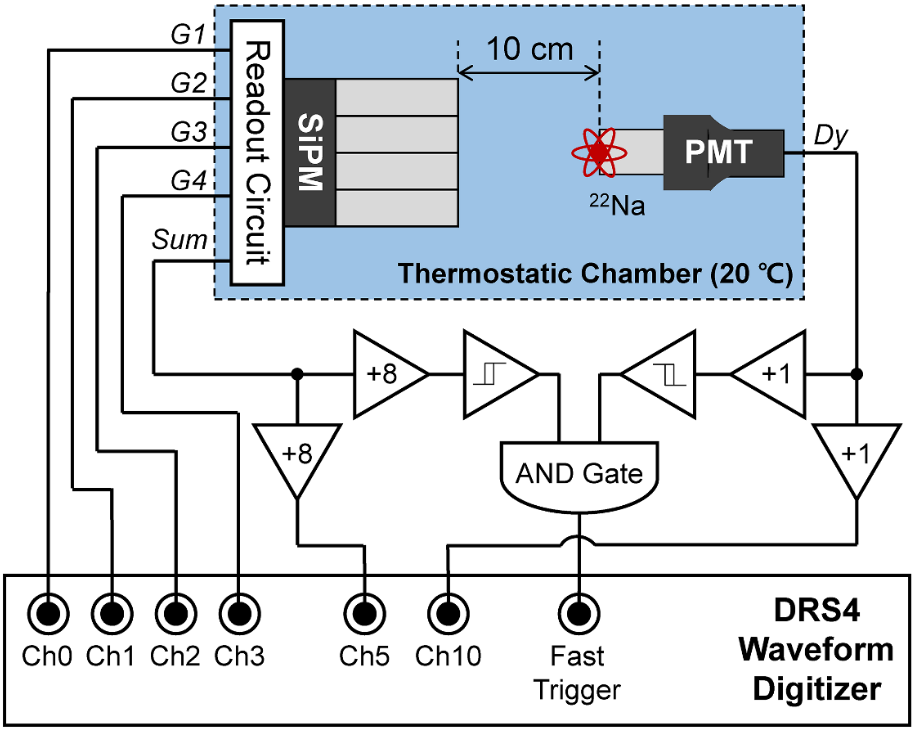

Figure 2. Experimental setup used in this study. The SiPM array was thermally regulated inside a thermostatic chamber at a fixed temperature of 20 °C. The four pulse train outputs (i.e. *G1*, *G2*, *G3*, and *G4*) were directly fed into a DRS4 digitizer. The *Sum* signal was replicated using a custom-made fan-in/fan-out module with an 8-fold signal amplification stage. One route was directly fed into the DRS4 digitizer and the other route was used for generating a coincidence trigger as an input for the DRS4 digitizer. The coincidence detection was performed using a ^{22}Na point source and PMT-based reference detector that features a STR of 220 ps FWHM.

the 2D flood map along the horizontal and vertical directions, respectively. E_{ij} corresponds to the energy deposited at each crystal element, where i and j are horizontal and vertical indices of the SiPM channels.

$$\hat{x} = \sum\nolimits_{j=1}^{4} \sum\nolimits_{i=1}^{4} E_{ij} \cdot i \tag{1}$$

$$\hat{y} = \sum\nolimits_{j=1}^{4} \sum\nolimits_{i=1}^{4} E_{ij} \cdot j \tag{2}$$

The energy deposited at each crystal was estimated using a time-over-threshold (TOT) technique (Shimazoe *et al* 2010). The relationship between the energy and TOT (i.e. the width of the digital pulses) is not linear but a surrogate function. Therefore, the TOT responses of the 16 SiPM anodes were calibrated by fitting the TOT photopeak values of ^{99m}Tc (140 keV), ^{22}Na (511 keV), and ^{137}Cs (662 keV) with a logarithmic function. The energy resolution was calculated using the calibrated TOT data per crystal.

The arrival time of annihilation photons was picked off from the *Sum* signal by applying a digital leading-edge discrimination method under an optimal threshold condition. To characterize the CRT value of the PET detector per crystal, the bias voltage was supplied only to the SiPM channel-of-interest at a time so that the *Sum* signal was generated only from a specified SiPM/LSO pair. This is because the DRS4 digitizer does not provide a function of simultaneous sampling of the SiPM signals with 1-GSPS and 5-GSPS sampling rates. The CRT measurement was then repeated 16 times for all the SiPM/LSO pairs within the 4×4 PET detector. The baseline correction of *Sum* signals was performed on a event-by-event basis by subtracting the mean value of 20 data samples before the signal onset. To minimize the quantization error, the *Sum* signal was 10-fold oversampled based on a cubic spline interpolation method. The energy window for the CRT analysis was 410 to 610 keV. The CRT value in coincidence with the reference detector ($\mathrm{CRT_{Det/Ref}}$) was estimated by fitting the time-difference histogram with a Gaussian curve. The CRT of the PET detector-of-interest ($\mathrm{CRT_{Det/Det}}$) was then calculated per crystal by unfolding the STR value ($\mathrm{STR_{Ref}}$) of the reference detector and subsequently multiplying by a factor of $\sqrt{2}$, as described in equation (3).

Table 1. Look-up table (LUT) for SiPM anode positioning.

Discharged SiPM Anode	Gamma Photon Arrival Time	Pulse Train Output Channel	Encoded Delay($\hat{u} = 250$ ns)	SiPM Anode Positioning LUT
A1			$0\hat{u}$	$(G1, t_\gamma + 0\hat{u})$
A2		$G1$	$1\hat{u}$	$(G2, t_\gamma + 1\hat{u})$
A3			$2\hat{u}$	$(G3, t_\gamma + 2\hat{u})$
A4			$3\hat{u}$	$(G4, t_\gamma + 3\hat{u})$
A5			$0\hat{u}$	$(G1, t_\gamma + 0\hat{u})$
A6		$G2$	$1\hat{u}$	$(G2, t_\gamma + 1\hat{u})$
A7			$2\hat{u}$	$(G3, t_\gamma + 2\hat{u})$
A8	t_γ		$3\hat{u}$	$(G4, t_\gamma + 3\hat{u})$
A9			$0\hat{u}$	$(G1, t_\gamma + 0\hat{u})$
A10		$G3$	$1\hat{u}$	$(G2, t_\gamma + 1\hat{u})$
A11			$2\hat{u}$	$(G3, t_\gamma + 2\hat{u})$
A12			$3\hat{u}$	$(G4, t_\gamma + 3\hat{u})$
A13			$0\hat{u}$	$(G1, t_\gamma + 0\hat{u})$
A14		$G4$	$1\hat{u}$	$(G2, t_\gamma + 1\hat{u})$
A15			$2\hat{u}$	$(G3, t_\gamma + 2\hat{u})$
A16			$3\hat{u}$	$(G4, t_\gamma + 3\hat{u})$

Table 2. Interaction type of annihilation photons within the PET detector.

Interaction Type	Number of Interactions	Energy Criterion	Occurence Rate
PE absorption	1	410 to 610 keV	51.70%
Scatter/escape	1	0 to 410 keV	36.47%
ICS	>1	410 to 610 keV	10.85%
ICS/escape	>1	0 to 410 keV	0.98%

$$\mathrm{CRT}_{\mathrm{Det/Det}} = \sqrt{2} \cdot \sqrt{\mathrm{CRT}_{\mathrm{Det/Ref}} - \mathrm{STR}^2_{\mathrm{Ref}}} \tag{3}$$

3. Results

3.1. ICS event identification

Figure 3 shows the representative signals of the pulse train outputs for PE absorption, scatter/escape, ICS, and ICS/escape events, respectively. The PE absorption (figure 3(a)) and scatter/escape events (figure 3(b)) are characterized by a single digital pulse with different TOT values. The deposited energy of PE absorption events falls into the energy window around the 511 keV photopeak, whereas that of the scatter/escape event falls outside the 511 keV photopeak window. The ICS events generate two or more digital pulses, where the sum of deposited energies falls into the energy window around the 511 keV photopeak (figure 3(c)). Multiple TOT pulses, whose energy sum is less than the lower bound of the energy window, were regarded as ICS/escape events (figure 3(d)).

Table 2 summarizes the interaction types of annihilation photons in the PET detector. The PE absorption events are represented as a single dot in the 2D flood map (figure 4(a)), whereas the ICS events generate cross-box patterns across the 2D flood map (figure 4(b)). The cross-box patterns are an indicator of ICS events occurred within the pixelated PET detectors. This is because the ICS events partially deposit their energies across multiple crystal elements, resulting in the positioning of ICS events somewhere between the crystal elements based on a center-of-gravity algorithm. The occurrence rate of ICS events for the 4×4 PET detector module with 3.2 mm-pitch LSO crystals was 10.85%.

3.2. PET detector performance

Figure 5 shows the performance of the PET detector. The TOT value that falls into the 511 keV photopeak window corresponded to 211 ± 6 ns per crystal, which did not exceed the pre-defined time-delay of 250 ns (figure 5(a)). The energy histogram (figure 5(c)) was generated to calculate energy resolution by converting the TOT histogram using a TOT-to-energy calibration curve (figure 5(b)). The energy resolution per crystal was $10.9 \pm 0.6\%$ (figure 5(d)). Figure 5(e) shows the sample time-difference histogram of the reference detector and PET detector-of-interest. The CRT for the PET detector-of-interest ($\mathrm{CRT}_{\mathrm{Det/Det}}$) was calculated as 285 ± 12 ps FWHM per crystal (figure 5(f)). Comparing the performance with the individual readout, the energy resolution was similar but the CRT was degraded by 25 ps FWHM on average using the proposed

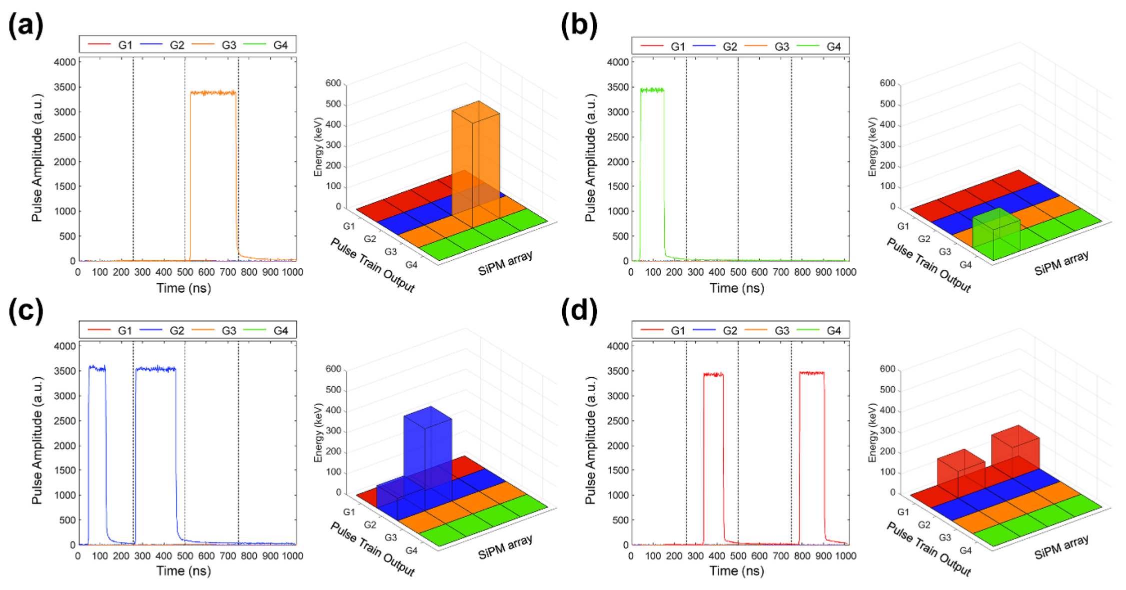

Figure 3. Representative signals from the pulse train outputs. (a) PE absorption event: a single digital pulse whose energy falls into the energy window around the 511 keV photopeak. (b) Scatter/escape event: a single digital pulse whose energy falls outside the 511 keV photopeak window. (c) ICS event: multiple digital pulses whose energy sum falls into the energy window around the 511 keV photopeak. (d) ICS/escape event: multiple digital pulses whose energy sum falls outside the 511 keV photopeak window.

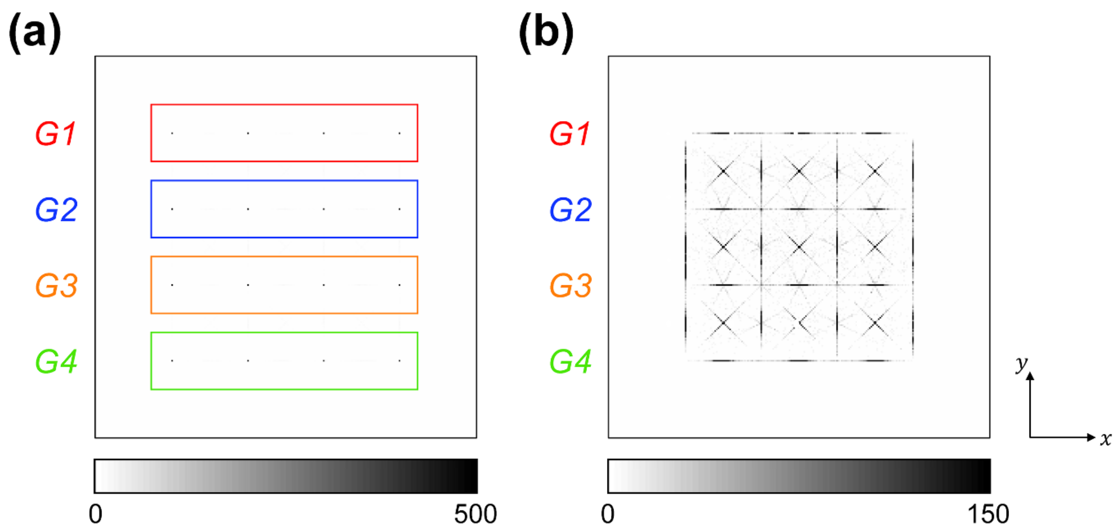

Figure 4. 2D flood maps for (a) PE absorption and (b) ICS events. The PE absorption events deposit their full energies only at a single crystal; and therefore, the PE absorption events are represented as a single dot in the 2D flood map. On the other hand, the ICS events undergo multiple Compton scattering and partially deposit their energies across multiple crystal elements. Accordingly, the ICS events result in cross-box patterns across the 2D flood map, given that the event positioning is based on a center-of-gravity algorithm.

method. No remarkable degradation in the PET detector performance was observed from the initial high count-rate measurement (i.e. multiple ^{22}Na point sources ($\sim$40 μCi) placing them at a 1 cm distance from the 4 $\times$ 4 PET detector module), yielding a similar energy resolution and CRT values.

4. Discussion

Previously, Cates *et al* (2017) proposed a similar SiPM readout approach to provide a scalable solution of SiPM multiplexing with a minimal CRT degradation for TOF PET applications. In their previous work, the position and energy information was encoded using the four corner signals from a resistive charge division network, which were subsequently digitalized and serialized into a single pulse train output using fast comparators and active delay chips. By using this method, however, it is difficult to identify the annihilation photons that underwent Compton scattering events across multiple crystal elements within a PET detector. This is because the resistive charge division network decodes the interacted position of ICS events

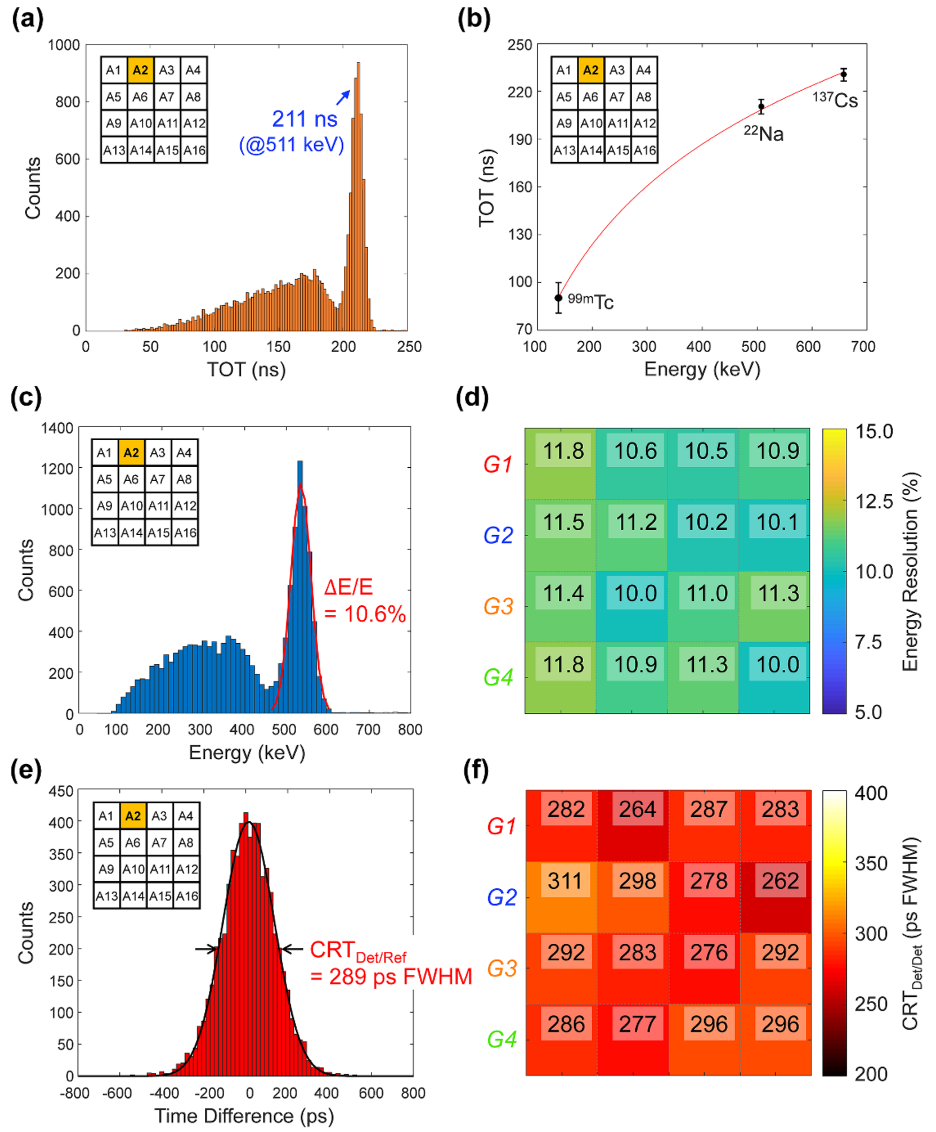

Figure 5. PET detector performances. (a) Sample TOT histogram. The TOT value around the 511 keV photopeak did not exceed the pre-defined time-delay of 250 ns. (b) Sample TOT-to-energy calibration curve. A curve fitting was performed with a logarithmic function using the TOT photopeak values of ^{99m}Tc (140 keV), ^{22}Na (511 keV), and ^{137}Cs (662 keV). (c) Sample energy histogram. (d) Energy resolution map per crystal. The average energy resolution was 10.9 ± 0.6%. (e) Time-difference histogram of the reference detector and PET detector-of-interest. (f) CRT map per crystal. The CRT for PET detector-of-interest ($CRT_{Det/Det}$) was calculated as 285 ± 12 ps FWHM.

somewhere between the two crystals based on a center-of-gravity algorithm. On the other hand, the proposed method individually handles every SiPM channel based on the pre-defined time-delays and four pulse train outputs; and therefore, the interacted position and deposited energy of the ICS events can be identified by analyzing the four pulse train outputs.

In the proposed method, the number of readout channels is same as that of typical PET detectors based on a charge division network (Goertzen *et al* 2013, Ko *et al* 2013, Park and Lee 2019). Therefore, we can achieve almost a 4-fold reduction of readout channels while preserving an inherent ICS event identification capability of the individual SiPM readout scheme. Fully digitalized timing and position signals of PET detectors based on the proposed SiPM readout method would potentially allow us to use field-programmable gate array (FPGA)-only back-end DAQ system (Won *et al* 2020) based on precise time-to-digital converters (TDCs) (Won *et al* 2016, Won and Lee 2016).

We expect better TOF capability by operating the SiPMs at a higher overvoltage; however, there existed a trade-off between good timing resolution and poor ICS event identification capability. We concluded that the increased number of after pulses in SiPM worsens the uncertainty of TOT-based energy measurement and subsequently degrades the accuracy of ICS event identification, especially in detecting Compton-scattered annihilation photons having low energies.

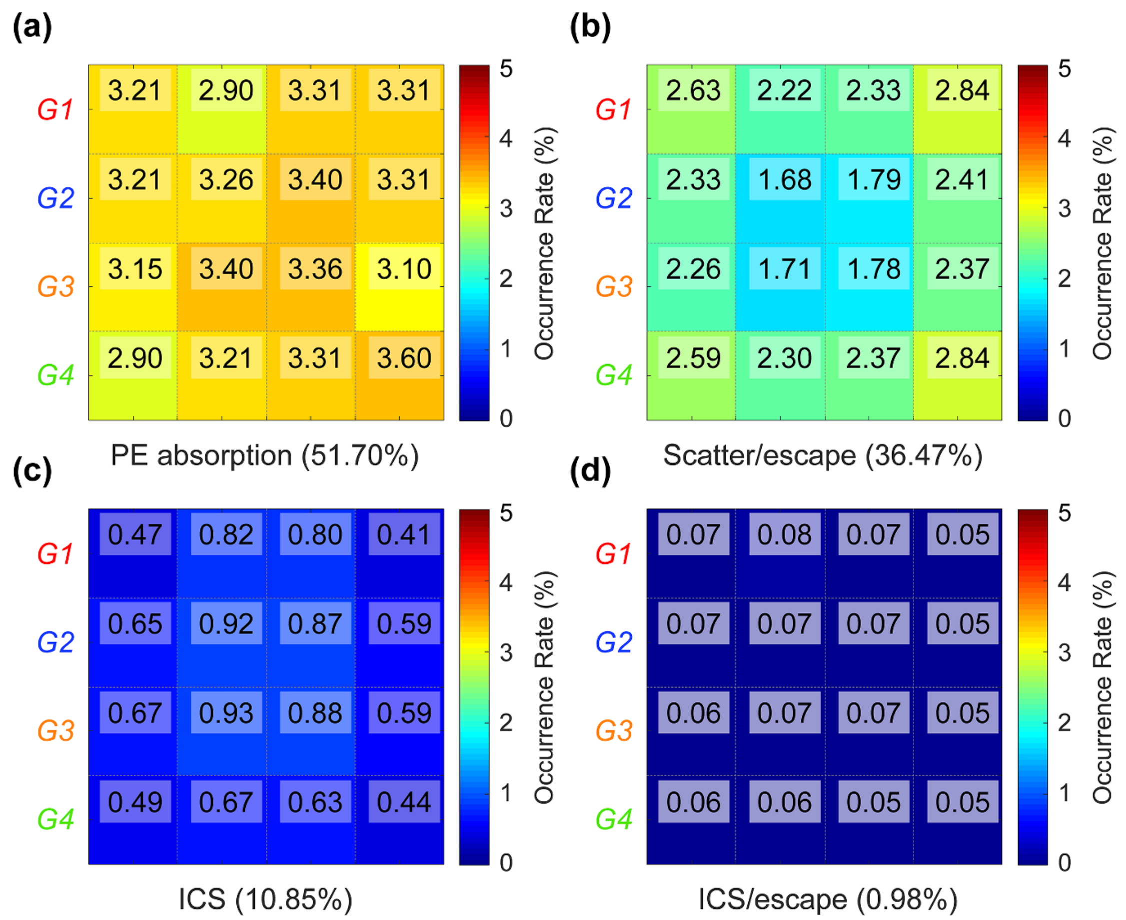

Figure 6. Probability distribution map of each interaction type of annihilation photons per crystal. (a) PE absorption, (b) Scatter/escape, (c) ICS, and (d) ICS/escape events.

Figure 6 shows the probability distribution map for each interaction type of annihilation photons per crystal. Here, about 30% of annihilation photons underwent Compton scattering events with a subsequent escape (i.e. scatter/escape events) from 12 boundary crystals (figure 6(b)). In a PET detector module larger than a 4 × 4 array, these 30% of scatter/escape events can be potentially identified as ICS events by detecting the partial energy deposition across multiple crystal elements at two adjacent PET detector modules. Accordingly, the total occurrence rate of ICS events will be subsequently increased for the larger PET detector module. In principle, the proposed method can be scaled up to identify ICS events occurred across two adjacent PET detector modules by individually recording the pulse train outputs from each PET detector module at a system-level. We plan to develop a proof-of-concept PET system that consists of multiple 4 × 4 detector modules using high-performance multichannel TDCs implemented within an FPGA (Won *et al* 2016) to demonstrate the scalability of the proposed method.

Unlike the conventional multiplexing techniques for SiPM arrays, the proposed method makes it possible to individually record the PET detector signals at a single SiPM level, thus being less critical from the deadtime issues. It is also worth noting that the deadtime issue of the proposed method is confined to a 4 × 4 crystal array, thereby attributing only a small portion of the total count-loss to a full-ring PET system at high activity, as discussed in Cates *et al* (2017).

Several different methods have been investigated to improve the quality of PET images using the identified ICS events. One simple approach is to eliminate the ICS events. Ritzer *et al* (2017) proposed an ICS event rejection method based on the measurement of light-spread distribution; however, one drawback of this approach is the loss of PET sensitivity and increase in statistical noise. Another approach is to recover the ICS events into the first interacted positions. A proportional method is a simple ICS event recovery algorithm that assigns the interacted position of ICS events only by proportionally weighting the counts recorded at each crystal element (Lage *et al* 2015, Lee *et al* 2018b, 2020). Other ICS event recovery algorithms seek the first interacted positions by analyzing the energy deposition of annihilation photons (Comanor *et al* 1996, Shao *et al* 1996, Ota *et al* 2017, Surti and Karp 2018) or by incorporating Compton kinematic information based on the Klein–Nishina formula (Rafecas *et al* 2003, Gillam *et al* 2014). Also, a deep-learning-based ICS event recovery method is interesting as the deep learning has proven its efficacy in many other biomedical signal and image processing fields (Park *et al* 2018b, Hegazy *et al* 2019, Hwang *et al* 2019, Akut 2019). We plan to further evaluate the contribution of the proposed method by applying the ICS event recovery algorithms into a proof-of-concept PET system that will be developed based on multiple 4×4 PET detector modules.

5. Summary and conclusions

In this work, we investigated a novel SiPM readout method for ICS event identification using the one-to-one coupled PET detector and demonstrated the feasibility of the proposed method. The proposed method successfully identified ICS events from other PE absorption or scatter/escape events. The occurrence rate of ICS events was 10.85% for the 4×4 PET detector module with 3.2 mm-pitch LSO crystals. The PET detector incorporated with the proposed SiPM readout scheme yielded a good detector performance with an energy resolution of $10.9 \pm 0.6\%$ and CRT of 285 ± 12 ps FWHM, respectively. Based on the results, we expect that the proposed method can be a useful solution for alleviating the readout burden of SiPM-based PET scanners with ICS event identification capability.

Acknowledgments

This work was supported by grants from the National Research Foundation of Korea (NRF) funded by the Korean Ministry of Science, ICT, and Future Planning (Grant No. NRF-2016R1A2B3014645).

ORCID iD

Jae Sung Lee https://orcid.org/0000-0001-7623-053X

References

Abbaszadeh S, Chinn G and Levin C S 2018 Positioning true coincidences that undergo inter-and intra-crystal scatter for a sub-mm resolution cadmium zinc telluride-based PET system *Phys. Med. Biol.* **63** 025012

Akut R 2019 FILM: finding the location of microaneurysms on the retina *Biomed. Eng. Lett.* **9** 497–506

Bruyndonckx P, Lemaître C, van Der Laan D J, Maas M, Schaart D, Yonggang W, Li Z, Krieguer M and Tavernier S 2006 Evaluation of machine learning algorithms for localization of photons in undivided scintillator blocks for PET detectors *IEEE Trans. Nucl. Sci.* **55** 918–24

Cates J W, Bieniosek M F and Levin C S 2017 Highly multiplexed signal readout for a time-of-flight positron emission tomography detector based on silicon photomultipliers *J. Med. Imaging* **4** 011012

Cherry S R and Dahlbom M 2004 PET: physics, instrumentation, and scanners *PET: Molecular Imaging and Its Biological Applications*, ed M E Phelps (Berlin: Springer) pp 1–124

Comanor K A, Virador P R G and Moses W 1996 Algorithms to identify detector Compton scatter in PET modules *IEEE Trans. Nucl. Sci.* **43** 2213–8

Gillam J E, Solevi P, Oliver J F, Casella C, Heller M, Joram C and Rafecas M 2014 Sensitivity recovery for the AX-PET prototype using inter-crystal scattering events *Phys. Med. Biol.* **59** 4065–83

Goertzen A L *et al* 2013 Design and performance of a resistor multiplexing readout circuit for a SiPM detector *IEEE Trans. Nucl. Sci.* **60** 1541–9

Hegazy M A, Cho M H, Cho M H and Lee S Y 2019 U-net based metal segmentation on projection domain for metal artifact reduction in dental CT *Biomed. Eng. Lett.* **9** 375–85

Hong S J, Kwon S I, Ito M, Lee G S, Sim K-S, Park K S, Rhee J T and Lee J S 2008 Concept verification of three-layer DOI detectors for small animal PET *IEEE Trans. Nucl. Sci.* **55** 912–7

Hwang D, Kang S K, Kim K Y, Seo S, Paeng J C, Lee D S and Lee J S 2019 Generation of PET attenuation map for whole-body time-of-flight 18F-FDG PET/MRI using a deep neural network trained with simultaneously reconstructed activity and attenuation maps *J. Nucl. Med.* **60** 1183–9

Ito M, Lee J P and Lee J S 2013 Timing performance study of new fast PMTs with LYSO for time-of-flight PET *IEEE Trans. Nucl. Sci.* **60** 30–37

Ko G B, Kim K Y, Yoon H S, Lee M S, Son J-W, Im H J and Lee J S 2016 Evaluation of a silicon photomultiplier PET insert for simultaneous PET and MR imaging *Med. Phys.* **43** 72–83

Ko G B, Yoon H S, Kwon S I, Lee C M, Ito M, Hong S J, Lee D S and Lee J S 2013 Development of a front-end analog circuit for multi-channel SiPM readout and performance verification for various PET detector designs *Nucl. Instr. Meth.* A **703** 38–44

Kuang Z *et al* 2018 Development of depth encoding small animal PET detectors using dual-ended readout of pixelated scintillator arrays with SiPMs *Med. Phys.* **45** 613–21

Kwon S I and Lee J S 2014 Signal encoding method for a time-of-flight PET detector using a silicon photomultiplier array *Nucl. Instr. Meth.* A **761** 39–45

Lage E, Parot V, Moore S C, Sitek A, Udías J M, Dave S R, Park M-A, Vaquero J and Herraiz J L 2015 Recovery and normalization of triple coincidences in PET *Med. Phys.* **42** 1398–410

Lee J P, Ito M and Lee J S 2011 Evaluation of a fast photomultiplier tube for time-of-flight PET *Biomed. Eng. Lett.* **1** 174–9

Lee J S 2012 Basic nuclear physics and instrumentation *Handbook of Nuclear Medicine and Molecular Imaging: Principles and Clinical Applications*, ed E Kim, D S Lee, U Tateishi and R P Baum (Singapore: World Scientific) pp 3–20

Lee M S, Kang S K and Lee J S 2018a Novel inter-crystal scattering event identification method for PET detectors *Phys. Med. Biol.* **63** 115015

Lee S, Kim K Y, Lee M S and Lee J S 2020 Recovery of inter-detector and inter-crystal scattering in brain PET based on LSO and GAGG crystals *Phys. Med. Biol.* **65** 195005

Lee S, Lee M S, Kim K Y and Lee J S 2018b Systematic study on factors influencing the performance of interdetector scatter recovery in small-animal PET *Med. Phys.* **45** 3551–62

Maas M C, Schaart D R, van der Laan D J, Bruyndonckx P, Lematre C, Beekman F J and van Eijk C W E 2009 Monolithic scintillator PET detectors with intrinsic depth-of-interaction correction *Phys. Med. Biol.* **54** 1893–908

Miyaoka R S and Lewellen T K 2000 Effect of detector scatter on the decoding accuracy of a DOI detector module *IEEE Trans. Nucl. Sci.* **47** 1614–9

Müller F, Schug D, Hallen P, Grahe J and Schulz V 2019 A novel DOI positioning algorithm for monolithic scintillator crystals in PET based on gradient tree boosting *IEEE Trans. Radiat. Plasma Med. Sci.* **3** 465–74

Ota R, Omura T, Yamada R, Miwa T and Watanabe M 2017 Evaluation of a sub-millimeter resolution PET detector with a 1.2 mm pitch TSV-MPPC array one-to-one coupled to LFS scintillator crystals and inter-crystal scatter studies with individual signal readout *IEEE Trans. Radiat. Plasma Med. Sci.* **1** 15–22

Park H, Ko G B and Lee J S 2017 Hybrid charge division multiplexing method for silicon photomultiplier based PET detectors *Phys. Med. Biol.* **62** 4390–405

Park H and Lee J S 2019 Highly multiplexed SiPM signal readout for brain-dedicated TOF-DOI PET detectors *Phys. Med.* **68** 117–23

Park H, Lee S, Ko G B and Lee J S 2018a Achieving reliable coincidence resolving time measurement of PET detectors using multichannel waveform digitizer based on DRS4 chip *Phys. Med. Biol.* **63** 24NT02

Park J, Hwang D, Kim K Y, Kang S K, Kim Y K and Lee J S 2018b Computed tomography super-resolution using deep convolutional neural network *Phys. Med. Biol.* **63** 145011

Phelps M E 2000 Positron emission tomography provides molecular imaging of biological processes *Proc. Natl. Acad. Sci.* **97** 9226–33

Pizzichemi M, Stringhini G, Niknejad T, Liu Z, Lecoq P, Tavernier S, Varela J, Paganoni M and Auffray E 2016 A new method for depth of interaction determination in PET detectors *Phys. Med. Biol.* **61** 4679–98

Pratx G and Levin C S 2009 Bayesian reconstruction of photon interaction sequences for high-resolution PET detectors *Phys. Med. Biol.* **54** 4065–83

Rafecas M, Böning G, Pichler B J, Lorenz E, Schwaiger M and Ziegler S I 2003 Inter-crystal scatter in a dual layer, high resolution LSO-APD positron emission tomograph *Phys. Med. Biol.* **48** 821–48

Ritzer C, Hallen P, Schug D and Schulz V 2017 Intercrystal scatter rejection for pixelated PET detectors *IEEE Trans. Radiat. Plasma Med. Sci.* **1** 191–200

Shao Y, Cherry S R, Siegel S and Silvermann R W 1996 A study of inter-crystal scatter in small scintillator arrays designed for high resolution PET imaging *IEEE Trans. Nucl. Sci.* **43** 1938–44

Shimazoe K, Takahashi H, Shi B, Furumiya T, Ooi J, Kumazawa Y and Murayama H 2010 Novel front-end pulse processing scheme for PET system based on pulse width modulation and pulse train method *IEEE Trans. Nucl. Sci.* **57** 782–6

Shinohara K, Suga M, Yoshida E, Nishikido F, Inadama N, Tashima H and Yamaya T 2014 Maximum likelihood estimation of inter-crystal events scattering events for light sharing PET detectors *IEEE Nuclear Science. Symp. Medical Imaging Conf. Record* pp 1–3

Siegel S, Silverman R W, Shao Y and Cherry S R 1996 Simple charge division readouts for imaging scintillator arrays using a multi-channel PMT *IEEE Trans. Nucl. Sci.* **43** 1634–41

Surti S and Karp J S 2018 Impact of event positioning algorithm on performance of a whole-body PET scanner using one-to-one coupled detectors *Phys. Med. Biol.* **63** 055008

Teimoorisichani M and Goertzen A L 2019 A study of inter-crystal scatter in dual-layer offset scintillator arrays for brain-dedicated PET scanners *Phys. Med. Biol.* **64** 115007

Won J Y, Ko G B, Kim K Y, Park H, Lee S, Son J-W and Lee J S 2020 Comparator-less PET data acquisition system using single-ended memory interface input receivers of FPGA *Phys. Med. Biol.* **65** 155007

Won J Y, Kwon S I, Yoon H S, Ko G B and Lee J S 2016 Dual-phase tapped-delay-line time-to-digital converter with on-the-fly calibration implemented in 40 nm FPGA *IEEE Trans. Biomed. Circ. Sys.* **10** 231–42

Won J Y and Lee J S 2016 Time-to-digital converter using a tuned-delay line evaluated in 28, 40, and 45 nm FPGAs *IEEE Trans. Instrum. Meas.* **65** 1678–89

Yamamoto S, Watabe H, Kanai Y, Watabe T, Kato K and Hatazawa J 2013 Development of an ultrahigh resolution Si-PM based PET system for small animals *Phys. Med. Biol.* **58** 7875–88

Yamaya T, Mitsuhashi T, Matsumoto T, Inadama N, Nishikido F, Yoshida E, Murayama H, Kawai H, Suga M and Watanabe M 2011 A SiPM-based isotropic-3D PET detector X'tal cube with a three-dimensional array of 1mm^3 crystals *Phys. Med. Biol.* **56** 6793–807

Zhang C, Sang Z, Wang X, Zhang X and Yang Y 2019 The effects of inter-crystal scattering events on the performance of PET detectors *Phys. Med. Biol.* **64** 205004